Revista de Metalurgia
April–June 2020, 56 (2), e167
ISSN-L: 0034-8570
https://doi.org/10.3989/revmetalm.167

Phase evolution of $Ba_{1-x}Eu_xTi_{1-x/4}O_3$ during the sintering process in air with high temperature in situ X-ray diffraction

Juan P. Hernández-Lara[a], Miguel Pérez-Labra[a,✉], José A. Romero-Serrano[b], Aurelio Hernández-Ramírez[b], Francisco R. Barrientos-Hernández[a], Ricardo Martínez-López[a], Víctor E. Reyes-Cruz[a], José A. Cobos-Murcia[a]

[a]Academic Area of Earth Sciences and Materials, Autonomous University of Hidalgo State. Road Pachuca- Tulancingo Km 4.5 Mineral de la Reforma, Zip Code 42184, Hidalgo, México
[b]Metallurgy and Materials Department, ESIQIE-IPN. UPALM, Zacatenco, Zip Code 07738, Ciudad de México, México

(✉Corresponding Author: miguelabra@hotmail.com)

Submitted: 22 November 2019; Accepted: 20 January 2020; Available On-line: 3 September 2020

ABSTRACT: The phase evolution of $Ba_{1-x}Eu_xTi_{1-x/4}O_3$ during the sintering process (heating and cooling) in the air with x = 0.0054, 0.0384, 0.1920, and 0.2689 mol% Eu_2O_3 was investigated by high temperature *in situ* X-ray diffraction in the range of temperature between 30 and 1200 °C. The samples were prepared mixing $BaCO_3$, TiO_2 and Eu_2O_3 powders using the solid-state method. The results obtained for the samples with x ≥ 0.2689 mol% Eu_2O_3 showed the cubic phase $BaTiO_3$ doped with Eu^{3+} at 900 °C. Below 500 °C the tetragonal ferroelectric phase $BaTiO_3$ doped with Eu^{3+} was detected. The secondary phase Ba_2TiO_4 was identified in the samples when heated to 1100°C with x = 0.0054, 0.0384 and 0.2689 mol% Eu_2O_3 and at 1200 °C for x = 0.1920 mol% Eu_2O_3. The secondary phases $Eu_2Ti_2O_7$ and Eu_2TiO_5 were identified during cooling in the temperature range of 1200 °C to room temperature for the sample with x = 0.1920 and 0.2689 mol% Eu_2O_3. The results of high-resolution scanning electron microscope (HRSEM) showed a wide grain-size distribution, a partially homogeneous microstructure and higher amounts of inter-granular porosity as well as a uniform incorporation and distribution of Ti, Ba and Eu in each sample.

KEYWORDS: $BaTiO_3$; Eu^{3+}; High temperature in situ X-Ray Diffraction; Sintering

Citation/Citar como: Hernández-Lara, J.P.; Pérez-Labra, M.; Romero-Serrano, J.A.; Hernández-Ramiréz, A.; Barrientos-Hernández, F.R.; Martínez-López, R.; Reyez-Cruz, V.E.; Cobos-Murcia, J.A. (2020). "Phase evolution of $Ba_{1-x}Eu_xTi_{1-x/4}O_3$ during the sintering process in air with high temperature in situ X-ray diffraction". *Rev. Metal.* 56(2): e167. https://doi.org/10.3989/revmetalm.167

RESUMEN: *Evolución de fases de $Ba_{1-x}Eu_xTi_{1-x/4}O_3$ durante el proceso de sinterizado en aire con Difracción de Rayos X in situ a alta temperatura***.** La evolución de fases de $Ba_{1-x}Eu_xTi_{1-x/4}O_3$ durante el proceso de sinterizado (calentamiento-enfriamiento) en aire con x = 0,0054; 0,0384; 0,1920 y 0,2689 mol% Eu_2O_3 fue investigada por Difracción de Rayos X *in situ* a alta temperatura en el rango de temperatura entre 30 y 1200 °C. Las muestras fueron preparadas mezclando $BaCO_3$, TiO_2 y Eu_2O_3 empleando el método de reacción en estado sólido. Los resultados para las muestras con x ≥ 0,2689 mol% Eu_2O_3 mostraron la fase cubica $BaTiO_3$ dopada con Eu^{3+} a 900 °C. Por debajo de 500 °C fue identificada la fase tetragonal ferroeléctrica $BaTiO_3$ dopada con Eu^{3+}. La fase secundaria Ba_2TiO_4 fué identificada en las muestras durante el calentamiento a 1100 °C con x = 0.0054, 0.0384 y 0.2689 mol% Eu_2O_3 y a 1200 °C para x = 0.1920 mol% Eu_2O_3. Las fases secundarias $Eu_2Ti_2O_7$ y Eu_2TiO_5 fueron identificadas durante el enfriamiento en el rango de temperatura de 1200 °C a temperatura ambiente para la muestra con x = 0.1920 y 0.2689 mol% Eu_2O_3. Los resultados de microscopía electrónica de barrido mostraron una amplia distribución de tamaño de grano, una microestructura parcialmente homogénea y altas cantidades de porosidad intergranular, así como una uniforme incorporación y distribución de Ti, Ba y Eu en cada muestra.

PALABRAS CLAVE: $BaTiO_3$; Difracción de Rayos-X in situ a alta temperatura; Eu^{3+}; Sinterización

ORCID ID: Juan P. Hernández-Lara (https://orcid.org/0000-0003-2937-7349); Miguel Pérez-Labra (https://orcid.org/0000-0001-9882-6932); José A. Romero-Serrano (https://orcid.org/0000-0001-9324-5602); Aurelio Hernández-Ramírez (https://orcid.org/0000-0002-1901-618X); Francisco R. Barrientos-Hernández (https://orcid.org/0000-0001-5459-7162); Ricardo Martínez-López (https://orcid.org/0000-0003-2294-4064); Víctor E. Reyes-Cruz (https://orcid.org/0000-0003-2984-850X); José A. Cobos-Murcia (https://orcid.org/0000-0002-9946-5785)

1. INTRODUCTION

Undoped barium titanate ($BaTiO_3$) is a ferroelectric ceramic material with a perovskite lattice structure ABO_3, has a relative permittivity of approximately 7000 at room temperature, this property allows us to use it in a wide variety of electronic devices. The solid $BaTiO_3$ can exist in five phases, listing from high temperature to low temperature: hexagonal, cubic, tetragonal, orthorhombic, and rhombohedral crystal structure (Moulson and Herbert, 1990). The undoped $BaTiO_3$ powders are usually obtained by solid-state reactions among mixed oxides (Templeton and Pask, 1959; O'Bryan Jr. and Thomson Jr., 1974; Beauger *et al.*, 1983a; Beauger *et al.*, 1983b; Amin *et al.*, 1983; Beauger *et al.*, 1984; Mutin and Niepce, 1984; Hilton and Frost, 1992; Viviani *et al.*, 1999; Veith *et al.*, 2000), also called dry reaction mixture of oxides. $BaTiO_3$ is obtained (Beauger *et al.*, 1983a; Veith *et al.*, 2000) in the reaction process (sintering) between TiO_2 and $BaCO_3$ at high temperatures. The empirical model for the solid-state reaction is according to (Beauger *et al.*, 1983b; Beauger *et al.*, 1984):

$$BaCO_3 \rightarrow \text{“BaO”} + CO_2 \quad (1)$$

$$\text{“BaO”} + TiO_2 \rightarrow BaTiO_3 \quad (2)$$

$$BaTiO_3 + \text{“BaO”} \rightarrow Ba_2TiO_4 \quad (3)$$

$$Ba_2TiO_4 + TiO_2 \rightarrow 2BaTiO_3 \quad (4)$$

It has been reported (Pavlovic *et al.*, 2008) that the barium orthotitanate (Ba_2TiO_4) phase (secondary phase), obtained at 800 °C during the sintering process reacts with the TiO_2 nucleus to form the consolidated phase $BaTiO_3$. In the process, the sintering temperature plays an important role, has been observed (Brzozowski and Castro, 2003) that high sintering temperatures generate coarse $BaTiO_3$ particles that are unsuitable for manufacturing fine grained ceramics. Also, if the nominal ratio of $BaCO_3/TiO_2$ is 1, the intermediate phases (secondary phases) or $BaCO_3$ can persist as an end-product and can modify greatly the electrical properties. On the other hand, it is well known that doping $BaTiO_3$ in A- and B-site, where the radius ionic is the primary parameter that determines the substitution site, have been extensively employed to modify and improve the electrical properties of undoped $BaTiO_3$ for different applications (Vijatović *et al.*, 2010). Nevertheless, the effect of dopants on the structure of $BaTiO_3$ crystal and the determination of the phases formed at different temperatures during the heating and cooling process has not received much attention. For example, with dopants such as Nb^{5+}, La^{3+} and Nd^{3+} the final structure becomes cubic when the dopant concentration exceeds ≈ 5 at% (Takada *et al.*, 1987). Moreover, when Y^{3+} dopants are incorporated at the Ba site (up to 1.5 at%) the final crystal structure is tetragonal, if the incorporation happens at the Ti site (up to 12 at%) and the Y^{3+} fraction is more than 6 at% and the final crystal structure becomes cubic (Zhi *et al.*, 1999).

Regarding grain size, the addition of donor dopants above the critical concentration (0.2 ± 0.5 at %) greatly inhibits grain growth (Buessem and Kahn, 1971; Belous *et al.*, 1998). It has been proven then that, besides controlling the electrical properties, the presence of dopants considerably affects the final microstructure of polycrystalline $BaTiO_3$.

The present paper only has aims to determine and explain the structural and phase transformation changes that occur during the heating and cooling process (sintering) of the $Ba_{1-x}Eu_xTi_{1-x/4}O_3$ solid solutions with x = 0.0054, 0.0384, 0.1920, 0.2689 mol% Eu_2O_3 as dopant using the high temperature *in situ* X-ray diffraction. This will be useful for the understanding of the relationship between the microstructure and doped $BaTiO_3$ properties, in this case with Eu^{3+}. The inclusion of europium into the host lattice of $BaTiO_3$ is rarely found in the literature. Europium is the most reactive rare-earth element, exhibits unusual metallurgical properties and has been reported as an efficient sensitizer of photoluminescence in perovskites and related materials (Lefevre *et al.*, 2018).

2. EXPERIMENTAL PROCEDURE

Four samples of solid solutions of Eu_2O_3 in $BaTiO_3$ were prepared by the solid state reaction route between $BaCO_3$ (Sigma-Aldrich, CAS No. 513-77-9, 99.9%), TiO_2 (Sigma-Aldrich, CAS No. 13463-67-7, 99.9%), and Eu_2O_3 (Sigma-Aldrich, CAS No. 1308-96-9 99.9%) using the equation $Ba_{1-x}Eu_xTi_{1-x/4}O_3$ with x = 0.0054, 0.0384, 0.1920 and 0.2689 mol% Eu_2O_3. A detailed experimental procedure for the synthesis was given previously (Barrientos Hernández *et al.*, 2014; Hernández Lara *et al.*, 2017), so only its summary will be presented here. The precursor powders were dried at 200 °C, before weighing. The mixture of the powders was decarbonated at 900 °C for 12 h with a heating rate of 5 °C · min^{-1}. Subsequently the samples were analyzed in a Panalytical X-ray diffractometer model Empyrean (Malvern Panalytical, Royston, United Kingdom), coupling with temperature chamber Anton Paar (HTK1200N. Anton Paar GmbH, Graz, Austria) applying a heating and cooling rate of 5 °C · min^{-1}. The X-Ray patterns were acquired at 30, 300, 400, 500, 700, 900, 1100 and 1200 °C during heating. Before the acquiring each X-Ray patterns the temperature was held for 30 min. Also, X-Ray patterns were obtained during the cooling process of the samples at 900, 700, 500 and 25 °C. Finally, the morphological studies and distribution

of Ti, Ba and Eu in the samples were performed in a high-resolution scanning electron microscope (HRSEM) JEOL 6701F (JEOL LTD, Tokyo, Japan).

3. RESULTS AND DISCUSSION

3.1. High temperature in situ X-Ray Diffraction

High temperature *in situ* X-ray diffraction is a method used in many research fields of materials science, chemical and pharmaceutical industries, metallurgy, geology, archeometry, or planetary science (Chung *et al.*, 1994). In this study, the technique was applied to determine the structural and phase transformation changes that occur during the heating and cooling process of the samples $Ba_{1-x}Eu_xTi_{1-x/4}O_3$ with x = 0.0054, 0.0384, 0.1920 and 0.2689 mol% Eu_2O_3. Figure 1 shows the X-Ray patterns acquired at 30, 300, 400, 500, 700, 900, 1100 and 1200 °C for the sample with x = 0.0054 mol% Eu_2O_3 during the heating (sintering process). This Figure also shows the results acquired at 900, 700, 500 and 25 °C during the cooling process. Before each acquisition, as mentioned already, the temperature was stabilized for 30 min. Similarly, Table 1 shows the identified events at each temperature. Figure 2 shows the results of high temperature in situ X-ray diffraction for $Ba_{1-x}Eu_xTi_{1-x/4}O_3$ powders, with x = 0.0384 mol% Eu_2O_3 during heating and cooling and Table 2 shows the events identified at each temperature for this composition.

Firstly, it should be noted in Table 1, equation 7, that $BaTiO_3$ is refers to the barium titanate phase doped with Eu^{3+}. Owing to ionic radius of Eu^{3+} ion equal to 0.947 Å (for coordination number equal to 6), which is between those of Ba^{2+} ion equal to

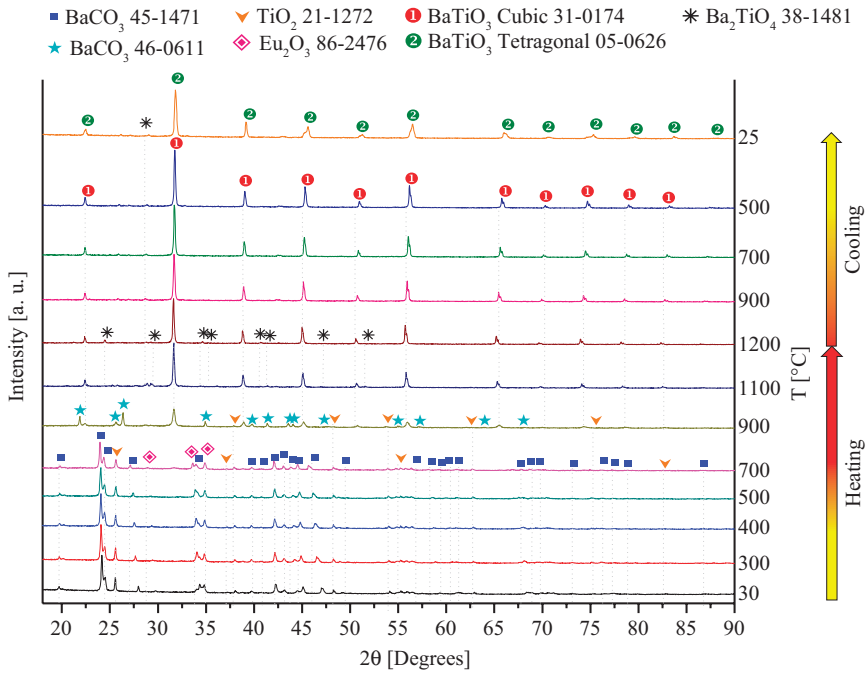

FIGURE 1. X-ray thermodiffraction for $Ba_{1-x}Eu_xTi_{1-x/4}O_3$ powders, x = 0.0054 mol% Eu_2O_3. Heating and cooling.

TABLE 1. Events identified at each temperature during heating and cooling for $Ba_{1-x}Eu_xTi_{1-x/4}O_3$ powders, x = 0.0054 mol% Eu_2O_3

T (°C)	Event	Equation
30-700	$BaCO_{3(O)} + TiO_2 + Eu_2O_3 \rightarrow BaCO_{3(O)} + TiO_2 + Eu_2O_3$	(6)
900	$BaCO_{3(O)} + 3TiO_2 + Eu_2O_3 \rightarrow BaCO_{3(H)} + TiO_2 + BaTiO_{3(C)}$	(7)
1100-1200	$2BaCO_{3(H)} + TiO_2 + 2\,BaTiO_{3(C)} \rightarrow 2\,BaTiO_{3(C)} + Ba_2TiO_4 + 2CO_2\uparrow$	(8)
1200-500	$BaTiO_{3(C)} + Ba_2TiO_4 \rightarrow BaTiO_{3(C)} + Ba_2TiO_4$	(9)
500-25	$BaTiO_{3(C)} + Ba_2TiO_4 \rightarrow BaTiO_{3(T)} + Ba_2TiO_4$	(10)

(O) = Orthorhombic, (H)= Hexagonal, (C)= Cubic, (T)= Tetragonal

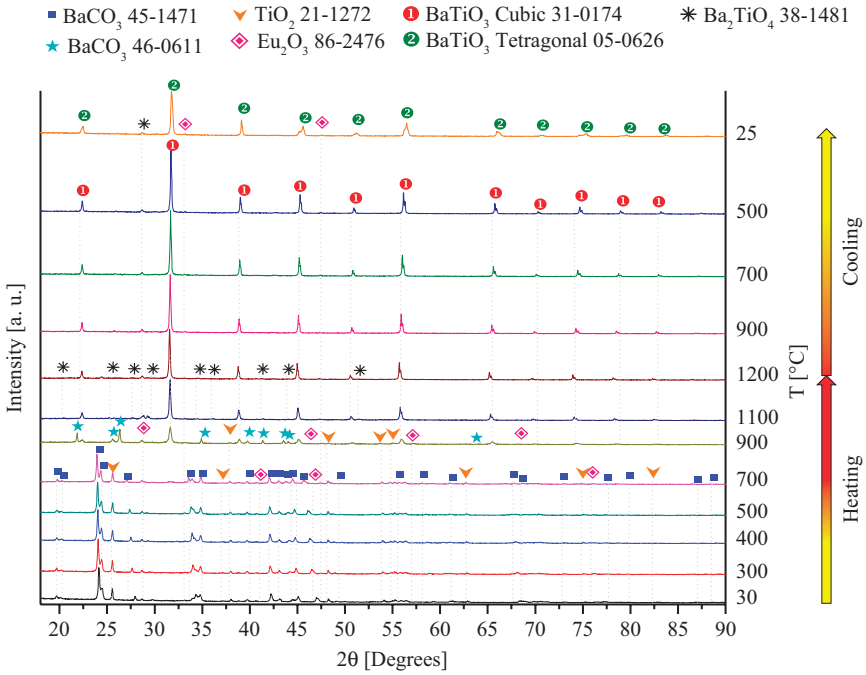

FIGURE 2. X-ray thermodiffraction for $Ba_{1-x}Eu_xTi_{1-x/4}O_3$ powders, x = 0.0384 mol% Eu_2O_3. Heating and cooling.

TABLE 2. Events identified at each temperature during heating and cooling for $Ba_{1-x}Eu_xTi_{1-x/4}O_3$ powders powders, x = 0.0384 mol% Eu_2O_3

T (°C)	Event	Equation
30-700	$BaCO_{3(O)} + TiO_2 + Eu_2O_3 \rightarrow BaCO_{3(O)} + TiO_2 + Eu_2O_3$	(11)
900	$2BaCO_{3(O)} + 2TiO_2 + Eu_2O_3 \rightarrow BaCO_{3(H)} + TiO_2 + Eu_2O_3 + BaTiO_{3(C)} + CO_2\uparrow$	(12)
1100-1200	$2BaCO_{3(H)} + TiO_2 + Eu_2O_3 + BaTiO_{3(C)} \rightarrow BaTiO_{3(C)} + Eu_2O_3 + Ba_2TiO_4 + 2CO_2\uparrow$	(13)
900-500	$BaTiO_{3(C)} + Eu_2O_3 + Ba_2TiO_4 \rightarrow BaTiO_{3(C)} + Eu_2O_3 + Ba_2TiO_4$	(14)
25	$BaTiO_{3(C)} + Eu_2O_3 + Ba_2TiO_4 \rightarrow BaTiO_{3(T)} + Eu_2O_3 + Ba_2TiO_4$	(15)

(O) = Orthorhombic, (H)= Hexagonal, (C)= Cubic, (T)= Tetragonal

1.61 Å (for coordination number equal to 12) and Ti^{4+} ion equal to 0.605 Å (for coordination number equal to 6), Eu^{3+} can occupy either A or B site in the ABO_3 compounds, depending on Ba/Ti mole ratio (Takada *et al.*, 1987; Dunbar *et al.*, 2004; Mitic *et al.*, 2010; Zhang and Hao, 2013). Then, if Eu^{3+} is added to $BaTiO_3$ the following reaction would take place (Chan *et al.*, 1986):

$$Eu_2O_3 \text{ (in } BaTiO_3) \rightarrow 2Eu_{Ti} + 2O_o + (1/2)\, O_2(g) + 2e' \quad (5)$$

It can be observed from Fig. 1 and Fig. 2 that during the sintering process for $Ba_{1-x}Eu_xTi_{1-x/4}O_3$ powders, with x = 0.0054 and x = 0.0384 mol % Eu_2O_3 in the temperature range 30 – 700 °C, the precursor powders did not react, (equation 6, Table 1). At 900 °C, a change in the crystal structure of the $BaCO_3$ precursor from orthorhombic (JCPDS 451471) to hexagonal (JCPDS 460611) could be identified. This change in crystal structure observed during heating process is characterized by an increase in cell volume of 304.42 Å to 496.27 Å (Antao and Hassan, 2007).

The formation of cubic $BaTiO_3$ (JCPDS 310174) was identified at 900 ºC at the angles in the X-Ray pattern 2θ ≈ 22.03°, 31.42°, 38.72°, 44.89°, 50.61°, 55.87°, 65.52°, 69.93°, 74.39°, 78.60° and 82.94°, together with the unreacted precursor powders, namely: hexagonal $BaCO_3$ (JCPDS 460611), TiO_2 (JCPDS 211272) for x = 0.0054 mol% Eu_2O_3 and Eu_2O_3 (JCPDS 862476) for x = 0.0384 mol% Eu_2O_3. It was observed that the cubic phase $BaTiO_3$ remained stable during heating up to 1200 °C and during the cooling process up to 500 °C. Down from 500 °C the tetragonal ferroelectric phase $BaTiO_3$ (JCPDS 050626) was identified. Subsequently this

phase remained stable until room temperature was reached for both compositions of Eu_2O_3.

It can also be observed in Figs. 1 and 2 that the formation of the secondary phase, barium orthotitanate (Ba_2TiO_4) JCPDS 381481, during the heating process was identified at 1100 °C with the angles in the X-Ray pattern at 2θ ≈ 25.18°, 28.86°, 29.12°, 34.79°, 36.09°, 40.69°, 41.54°, 47.32°, and 51.99°, this phase remained stable during the heating process up to 1200°C and during cooling to room temperature (2θ ≈ 29.12°).

The final structure observed consisted of the phases $BaTiO_3$ (JCPDS 050626) and Ba_2TiO_4 (JCPDS 381481) for the sample with x = 0.0054 mol% Eu_2O_3 (equation 10, Table 1) and $BaTiO_3$ (JCPDS 050626), Ba_2TiO_4 (JCPDS 381481) and Eu_2O_3 (JCPD 862476) (equation 15, Table 2) for the sample with x = 0.0384 mol% Eu_2O_3.

It has been recently reported (Sahmi *et al.*, 2019) that the phase barium orthotitanate (Ba_2TiO_4) crystallizes in a monoclinic perovskite structure and it finds applications in environmental protection. Further, Ba_2TiO_4 exhibits electrochemical stability when it is subjected to high electrical current values., its easy synthesis by chemical route increases the active surface area, resulting in enhanced photo activity with a high mineralization degree.

Figure 3 and 4 show the result corresponding to samples with x = 0.1920 and x = 0.2689 mol% Eu_2O_3, respectively, and in Tables 3 and 4, the events identified in each temperature. In the heating process, in the temperature range of 30 to 700 °C, similar to the results obtained for compositions with x = 0.0054 and x = 0.384 mol% Eu_2O_3, no changes in the composition of the precursor powders were observed. At 900 °C the phases present in both samples were similar to those identified in the sample with x = 0.0384 mol% Eu_2O_3. Cubic $BaTiO_3$ as well as unreacted precursor Eu_2O_3 were observed in the sample with x = 0.1920 mol% Eu_2O_3 at 1100 °C during the heating process, at this same temperature, for the sample with x = 0.2689 mol% Eu_2O_3 (Fig. 4, Table 4 equation 23), and due to the excess of the dopant precursor Eu_2O_3 the presence of secondary phases: pyrochlore $Eu_2Ti_2O_7$ (JCPD 231072) and orthorhombic Eu_2TiO_5 (JCPD 221100) together with phase Ba_2TiO_4 were observed, besides remnants of Eu_2O_3. For the sample with x = 0.1920 mol% Eu_2O_3 (Fig. 3) the formation of the secondary phases $Eu_2Ti_2O_7$, Eu_2TiO_5 and Ba_2TiO_4 together with the unreacted precursor Eu_2O_3 and the cubic $BaTiO_3$ phase were identified during the cooling process in the temperature range from 1200 °C to room temperature. This last event (Equation 19, Table 3) is similar to that identified for the sample with x = 0.2689 mol% Eu_2O_3 in the same temperature range, but the surplus precursor identified in this case was TiO_2. (Equation 24-25, Table 4).

Finally, the crystal structure change of cubic $BaTiO_3$ to tetragonal ferroelectric phase $BaTiO_3$ was identified at temperatures ≥ 500 °C during the cooling process. The excess dopant precursor Eu_2O_3

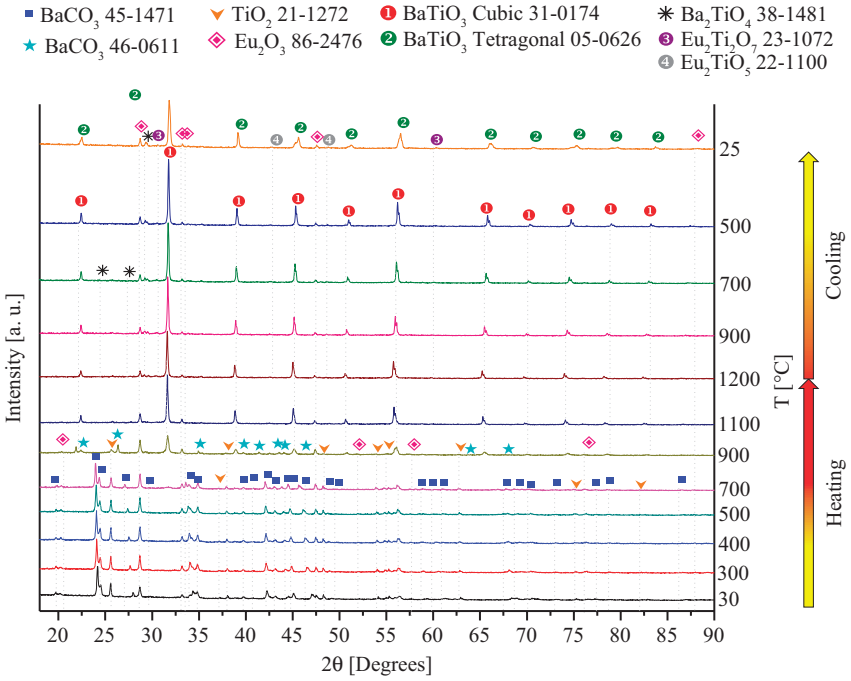

FIGURE 3. X-ray thermodiffraction for $Ba_{1-x}Eu_xTi_{1-x/4}O_3$ powders, x = 0.1920 mol% Eu_2O_3. Heating and cooling.

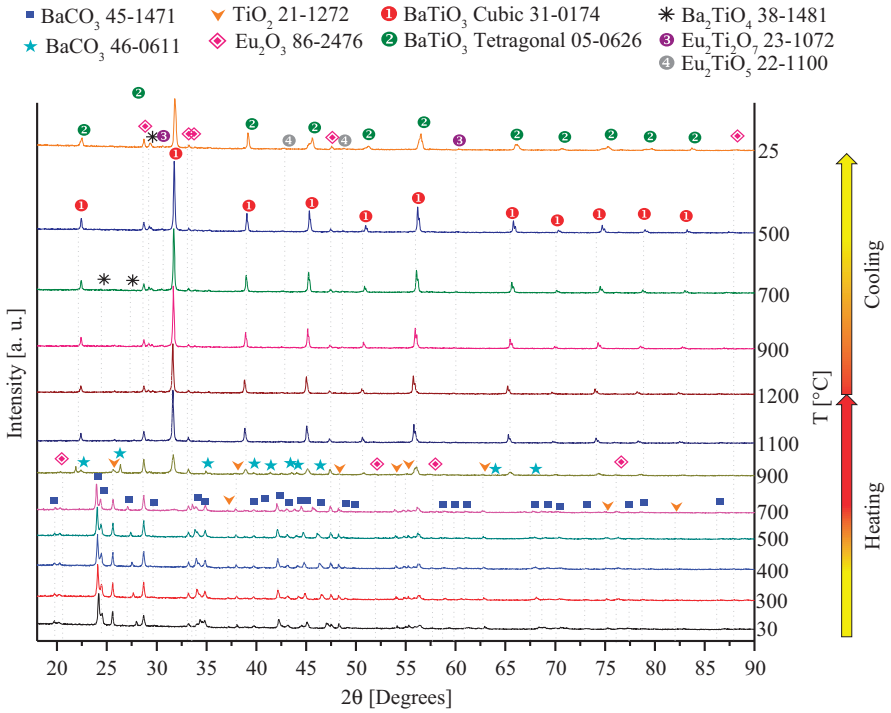

FIGURE 4. X-ray thermodiffraction for $Ba_{1-x}Eu_xTi_{1-x/4}O_3$ powders, x = 0.2689 mol% Eu_2O_3. Heating and cooling.

TABLE 3. Events identified at each temperature during heating and cooling for $Ba_{1-x}Eu_xTi_{1-x/4}O_3$ powders, x = 0.1920 mol% Eu_2O_3

T (°C)	Event	Equation
30-700	$BaCO_{3(O)} + TiO_2 + Eu_2O_3 \rightarrow BaCO_{3(O)} + TiO_2 + Eu_2O_3$	(16)
900	$2BaCO_{3(O)} + 2TiO_2 + Eu_2O_3 \rightarrow BaCO_{3(H)} + TiO_2 + Eu_2O_3 + BaTiO_{3(C)} + CO_2\uparrow$	(17)
1100	$BaCO_{3(H)} + TiO_2 + Eu_2O_3 + BaTiO_{3(C)} \rightarrow 2BaTiO_{3(C)} + Eu_2O_3 + CO_2\uparrow$	(18)
1200-500	$7BaTiO_{3(C)} + 3Eu_2O_3 \rightarrow BaTiO_{3(C)} + Eu_2O_3 + 3Ba_2TiO_4 + Eu_2Ti_2O_7 + Eu_2TiO_5$	(19)
25	$BaTiO_{3(C)} + Eu_2O_3 + Ba_2TiO_4 + Eu_2Ti_2O_7 + Eu_2TiO_5 \rightarrow BaTiO_{3(T)} + Eu_2O_3 + Ba_2TiO_4 + Eu_2Ti_2O_7 + Eu_2TiO_5$	(20)

(O) = Orthorhombic, (H)= Hexagonal, (C)= Cubic, (T)= Tetragonal

TABLE 4. Events identified at each temperature during heating and cooling for $Ba_{1-x}Eu_xTi_{1-x/4O3}$ powders, x = 0.2689 mol% Eu_2O_3

T (°C)	Event	Equation
30–700	$BaCO_{3(O)} + TiO_2 + Eu_2O_3 \rightarrow BaCO_{3(O)} + TiO_2 + Eu_2O_3$	(21)
900	$2BaCO_{3(O)} + 2TiO_2 + Eu_2O_3 \rightarrow BaCO_{3(H)} + TiO_2 + Eu_2O_3 + BaTiO_{3(C)} + CO_2\uparrow$	(22)
1100	$2BaCO_{3(H)} + 5TiO_2 + 3Eu_2O_3 + BaTiO_{3(C)} \rightarrow BaTiO_{3(C)} + Ba_2TiO_4 + TiO_2 + Eu_2O_3 + Eu_2Ti_2O_7 + Eu_2TiO_5 + 2CO_2\uparrow$	(23)
1200-500	$BaTiO_{3(C)} + Ba_2TiO_4 + 2TiO_2 + Eu_2O_3 + Eu_2Ti_2O_7 + Eu_2TiO_5 \rightarrow BaTiO_{3(C)} + Ba_2TiO_4 + TiO_2 + Eu_2Ti_2O_7 + 2Eu_2TiO_5$	(24)
25	$BaTiO_{3(C)} + Ba_2TiO_4 + TiO_2 + Eu_2Ti_2O_7 + Eu_2TiO_5 \rightarrow BaTiO_{3(T)} + Ba_2TiO_4 + TiO_2 + Eu_2Ti_2O_7 + Eu_2TiO_5$	(25)

(O) = Orthorhombic, (H)= Hexagonal, (C)= Cubic, (T)= Tetragonal

caused the formation of secondary phases consolidated with europium in its structure and remnants of TiO_2 (Fig. 4).

Regarding the secondary phases that were identified, it has been found that lanthanides or their oxide compounds have relatively large thermal neutron absorption cross sections, and hence compounds of europium, dysprosium, and gadolinium, including $Eu_2Ti_2O_7$ and Eu_2TiO_5, have been considered as potential candidates for use as control rod materials in nuclear reactors (Syamala *et al.*, 2008; Glerup *et al.*, 2001). The secondary phase $Eu_2Ti_2O_7$, which crystallize in the face-centered cubic pyrochlore structure with the general formula $RE_2Ti_2O_7$ (RE = rare earth element) occupies an exceptional position in the field of materials for spintronic devices (Glerup *et al.*, 2001).

3.2. Morphology and microstructure

The samples obtained after the heating and cooling process were analyzed by scanning electron microscopy (SEM-EDS). Figures 5 and 6 shows the X-ray mapping images of O, Ti, Ba and Eu elements for the samples with x = 0.0054 mol% Eu_2O_3 and with x = 0.2689 mol% Eu_2O_3, in the figure are also shown the compositions obtained by SEM-EDS semi-quantitative method. The X-ray mapping evidence a contrast along the element concentration gradient. So, in the X-ray image for europium, the bright areas correspond to europium-rich zones and the dark areas correspond to europium-poor zones. The X-ray mapping images show a uniform distribution of Ti, Ba and Eu in the sample. The incorporation of Eu^{3+} ions into the $BaTiO_3$ system could greatly manifest dielectric properties and can find immense scope in electronic elements including ceramic capacitors (Hernández Lara *et al.*, 2017).

The microstructures of samples with x = 0.0054, 0.0384, 0.1920, and 0.2689 mol% Eu_2O_3 are in Fig. 7, all the analyzed samples reveal similar grain sizes with a partially homogeneous microstructure and higher amounts of inter-granular porosity which was attributed to the behavior of Eu^{3+} in the $BaTiO_3$ phase. It could be observed that the amount of Eu^{3+} at the sample slightly affect the microstructures, which were characterized as subrounded grains with a wide grain-size distribution, between 0.28 and 2.13 μm for x = 0.0054 mol% Eu_2O_3 (Fig. 7a), 0.25 and 2.33 μm for x = 0.0384 mol% Eu_2O_3 (Fig. 7b), 0.58 and 3.66 mm for x = 0.1920 mol% Eu_2O_3

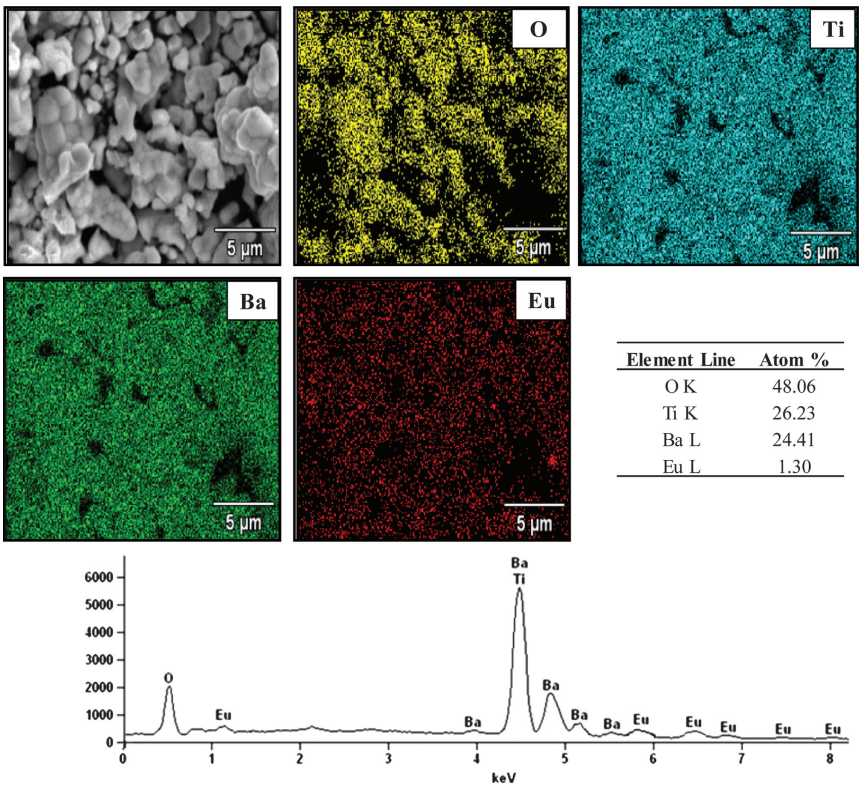

FIGURE 5. X-ray mapping images and EDS analysis of O, Ti, Ba and Eu elements for the $Ba_{1-x}Eu_xTi_{1-x/4}O_3$ sample, x = 0.0054 mol% Eu_2O_3.

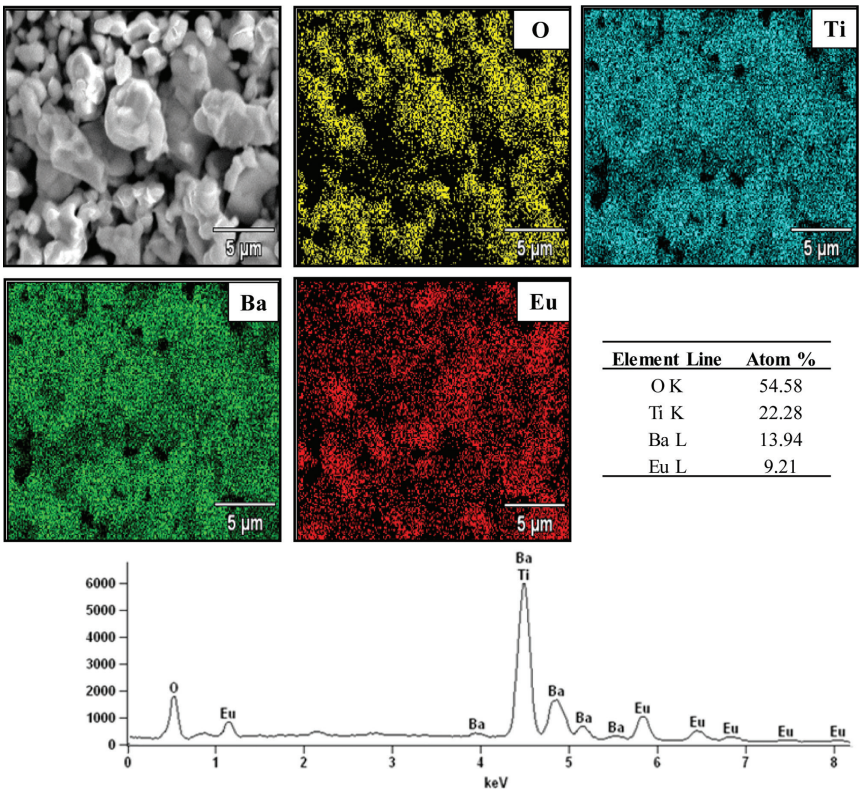

FIGURE 6. X-ray mapping images and EDS analysis of O, Ti, Ba and Eu elements for the $Ba_{1-x}Eu_xTi_{1-x/4}O_3$ sample, x = 0.2689 mol% Eu_2O_3.

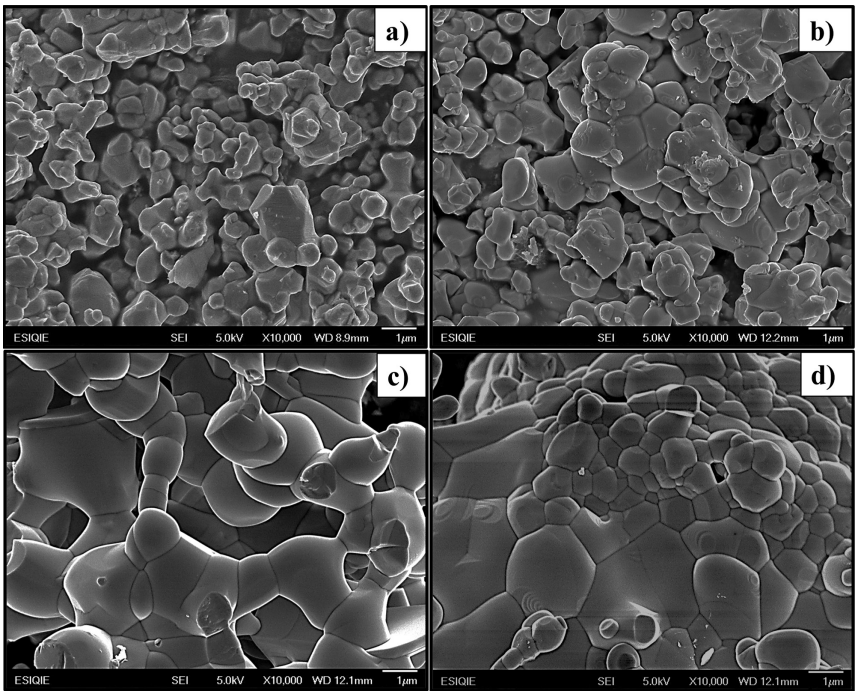

FIGURE 7. SEM micrographs for the $Ba_{1-x}Eu_xTi_{1-x/4}O_3$ samples: a) x = 0.0054 mol% Eu_2O_3, b) x = 0.0384 mol% Eu_2O_3, c) x = 0.1920 mol% Eu_2O_3 and d) x = 0.2689 mol% Eu_2O_3.

(Fig. 7c) and 0.23 and 4.03 μm for x = 0.2689 mol% Eu_2O_3 (Fig. 7d). Similar structures were reported in the study of the structural evolution $BaTiO_3$ doped with Gd^{3+}(Hernández Lara *et al.*, 2017).

4. CONCLUSIONS

- In this paper, the phase equilibria during the sintering process in the air of $Ba_{1-x}Eu_xTi_{1-x/4}O_3$ solid solutions with x = 0.0054, 0.0384, 0.1920, and 0.2689 mol% Eu_2O_3 were investigated by high temperature *in situ* X-ray diffraction. The X-Ray patterns showed the formation of the cubic phase $BaTiO_3$ at 900 °C in the samples with x ≥ 0.2689 mol% Eu_2O_3, this phase remained stable during heating up to 1200 °C and during cooling to 500 °C. Below this temperature the tetragonal ferroelectric phase $BaTiO_3$ was identified. The secondary phase Ba_2TiO_4 during heating was observed at 1100 °C in samples with x = 0.0054, 0.0384 and 0.2689 mol% Eu_2O_3 and at 1200 °C for the sample with x =0.1920 mol% Eu_2O_3, this phase remained stable during heating up to 1200 °C and during cooling to room temperature. The secondary phases $Eu_2Ti_2O_7$, and Eu_2TiO_5 were identified in the temperature range from 1200 °C to room temperature during the cooling process for the sample with x = 0.1920 and 0.2689 mol% Eu_2O_3 with surpluses of Eu_2O_3 and TiO_2, respectively.
- The SEM-EDS results of the samples revealed granular structures with higher amounts of inter-granular porosity. The microstructures were characterized as subrounded grains with a wide grain-size distribution. The X-ray mapping images showed a uniform distribution of Ti, Ba and Eu in the sample.

ACKNOWLEDGMENTS

The authors are grateful to CONACyT-México for financial support.

REFERENCES

Amin, A., Spears, M., Kulwicki, B. (1983). Reaction of Anatase and Rutile with Barium Carbonate. *J. Am. Ceram. Soc.* 66 (10), 733–738. https://doi.org/10.1111/j.1151-2916.1983.tb10540.x.

Antao, S.M., Hassan, I. (2007). BaCO3: high-temperature crystal structures and the Pmcn→R3m phase transition at 811°C. *Phys. Chem. Minerals* 34, 573–580. https://doi.org/10.1007/s00269-007-0172-8.

Barrientos Hernández, F.R., Lira Hernández, I.A., Gómez Yáñez, C., Arenas Flores, A., Cabrera Sierra, R., Pérez Labra, M. (2014). Structural evolution of $Ba_8Ti_3Nb_4O_{24}$ from $BaTiO_3$ using a series of $Ba(Ti_{1-5x}Nb_{4x})O_3$ solid solutions. *J. Alloys Compd.* 583, 587–592. http://dx.doi.org/10.1016/j.jallcom.2013.09.016.

Beauger, A., Mutin, J., Niepce, J. (1983a) Synthesis reaction of metatitanate $BaTiO_3$. Part 1. *J. Mater. Sci.* 18, 3041–3046. https://doi.org/10.1007/BF00700786.

Beauger, A., Mutin, J., Niepce, J. (1983b). Synthesis reaction of metatitanate $BaTiO_3$. Part 2 Study of solid-solid reaction interfaces. *J. Mater. Sci.* 18, 3543–3550. https://doi.org/10.1007/BF00540726.

Beauger, A., Mutin, J., Niepce, J. (1984). Role and behaviour of orthotitanate Ba_2TiO_4 during the processing of $BaTiO_3$ based ferroelectric ceramics. *J. Mater. Sci.* 19, 195–210. https://doi.org/10.1007/BF02403126.

Belous, A.G., V'yunov, O.I., Khomenko, B.S. (1998). Microstructure and semiconducting properties of barium titanate containing heterovalent substituents on the titanium site. *Inorganic Materials* 34 (6), 597–601.

Brzozowski, E., Castro, M.S. (2003). Lowering the synthesis temperature of high-purity $BaTiO_3$ powders by modifications in the processing conditions. *Thermochim. Acta.* 398 (1–2), 123–129. https://doi.org/10.1016/S0040-6031(02)00353-2.

Buessem, W.R., Kahn, M. (1971). Efects of grain growth on the distribution of Nb in $BaTiO_3$ ceramics. *J. Am. Ceram. Soc.* 54 (9), 458–461. https://doi.org/10.1111/j.1151-2916.1971.tb12385.x.

Chan, H.M., Harmer, M.R., Smyth, D.M.L. (1986). Compensating Defects in Highly Donor-Doped $BaTiO_3$. *J. Am. Ceram. Soc.* 69 (6), 507–510. https://doi.org/10.1111/j.1151-2916.1986.tb07453.x.

Chung, D.D.L., DeHaven, P.W., Arnold, H., Ghosh, D. (1994). X-ray diffraction at elevated temperatures: a method for in situ process analysis. *J. Appl. Cryst.* 27, 441–442. https://doi.org/10.1107/S0021889893013809.

Dunbar, T.D., Warren, W.L., Tuttle, B.A., Randall, C.A., Tsur, Y. (2004). Electro paramagnetic resonance investigations of lanthanide-doped barium titanate: Dopant site occupancy. *J. Phys. Chem. B* 108, 908–917. https://doi.org/10.1021/jp036542v.

Glerup, M., Nielsen, O.F., Poulsen, F.W. (2001). The Structural Transformation from the Pyrochlore Structure, $A_2B_2O_7$, to the Fluorite Structure, AO_2, Studied by Raman Spectroscopy and Defect Chemistry Modeling. *J. Solid State Chem.* 160 (1), 25–32. https://doi.org/10.1006/jssc.2000.9142.

Hernández Lara, J.P., Pérez Labra, M., Barrientos Hernández, F.R., Romero Serrano, J.A., Ávila Dávila, E.O., Thangarasu, P., Hernández Ramirez, A. (2017). Structural Evolution and Electrical Properties of $BaTiO_3$ Doped with Gd^{3+}. *Mat. Res.* 20 (2), 538–542. http://dx.doi.org/10.1590/1980-5373-MR-2016-0606.

Hilton, A.D., Frost, R. (1992). Recent Developments in the Manufacture of Barium Titanate Powders. *Key Eng. Mater.* 66–67, 145–184. https://doi.org/10.4028/www.scientific.net/KEM.66-67.145.

Lefevre, G., Herfurth, A., Kohlmann, H., Sayede, A., Wylezich, T., Welinski, S., P. Vaz Duarte., Parker, S.F., Blach, J.F., Goldner, P., Kunkel, N. (2018). Electron-phonon coupling in luminescent europium doped hydride perovskites studied by luminescence spectroscopy, inelastic neutron scattering, and first-principle calculations. *J. Phys. Chem. C* 122, 10501–10509. https://doi.org/10.1021/acs.jpcc.8b01011.

Mitic, V.V., Nikolic, Z.S., Pavlovic, V.B., Paunovic, V., MilJovic, M., Jordovic, B., Zivkovic, L. (2010). Influence of rare-earth dopants on barium titanate ceramics microstructure and corresponding electrical properties. *J. Am. Ceram. Soc.* 93 (1), 132–137. https://doi.org/10.1111/j.1551-2916.2009.03309.x.

Moulson, A.J., Herbert, J.M. (1990). *Electroceramics: Materials, Properties, Applications.* Chapman & Hall, London.

Mutin, J.C., Niepce, J.C. (1984). About stoichiometry of polycrystalline $BaTiO_3$ synthesized by solid-solid reaction. *J. Mater. Sci. Lett*. 3, 591–592. https://doi.org/10.1007/BF00719620.

O'Bryan Jr., H., Thomson Jr., J. (1974). Phase Equilibria in the TiO_2-Rich Region of the System BaO-TiO_2. *J. Am. Ceram. Soc.* 57 (12), 522–526. https://doi.org/10.1111/j.1151-2916.1974.tb10801.x.

Pavlovic, V.P., Stojanovic, B.D., Pavlovic, V.B., Marinkovic-Stanojevic, Z., Živković, Lj., Ristic, M.M. (2008). Synthesis of $BaTiO_3$ from a Mechanically Activated $BaCO_3$-TiO_2 System. *Sci Sinter*. 40, 21–26. https://doi.org/10.2298/SOS0801021P.

Sahmi, A., Laib, R., Omeiri, S., Bensadok, K., Trari, M. (2019). Photoelectrochemical properties of Ba_2TiO_4 prepared by nitrate route. Application to electro-photocatalysis of phenobarbital mineralization by solar light. *J. Photoch. Photobio. A*. 372, 29–34. https://doi.org/10.1016/j.jphotochem.2018.12.003.

Syamala, K.V., Panneerselvam, G., Subramanian, G.G.S., Antony, M.P. (2008). Synthesis, characterization and thermal expansion studies on europium titanate (Eu_2TiO_5). *Thermochim. Acta* 475 (1–2), 76–79. https://doi.org/10.1016/j.tca.2008.05.008.

Takada, K., Chang, E., Smyth, D.M. (1987). Rare earth additions to $BaTiO_3$. *Advan. Ceram.* 19, 147–152.

Templeton, L., Pask, J. (1959). Formation of $BaTiO_3$ from $BaCO_3$ and TiO_2 in Air and in CO_2. *J. Am. Ceram. Soc.* 42, 212–216. https://doi.org/10.1111/j.1151-2916.1959.tb15455.x.

Veith, M., Mathur, S., Lecerf, N., Huch, V., Decker, T., Beck, H., Wiser, W., Haberkorn, R. (2000). Sol-Gel Synthesis of Nano-Scaled $BaTiO_3$, $BaZrO_3$ and $BaTi_{0.5}Zr_{0.5}O_3$ Oxides via Single-Source Alkoxide Precursors and Semi-Alkoxide Routes. *J. Sol–Gel Sci. Technol.* 17, 145–158. https://doi.org/10.1023/A:1008795419020.

Vijatović, M.M., Stojanovic´, B.D., Bobic´, J.D., Ramoska, T., Bowen, P. (2010). Properties of lanthanum doped $BaTiO_3$ produced from nanopowders. *Ceram. Int.* 36 (6), 1817–1824. https://doi.org/10.1016/j.ceramint.2010.03.010.

Viviani, M., Buscaglia, M.T., Nanni, P., Parodi, R., Gemme, G., Dacca, A. (1999). XPS investigation of surface properties of $Ba_{(1-x)}Sr_xTiO_3$ powders prepared by low temperature aqueous synthesis. *J. Eur. Ceram. Soc.* 19 (6–7), 1047–1051. https://doi.org/10.1016/S0955-2219(98)00371-9.

Zhang, Y., Hao, J. (2013). Color-tunable upconversion luminescence of Yb^{3+}, Er^{3+}, and Tm^{3+} tri-doped ferroelectric $BaTiO_3$ materials. *J. Appl. Phys.* 113 (18), 184112. https://doi.org/10.1063/1.4805050.

Zhi, J., Chen, A., Zhi, Y., Vilarinho, P.M., Baptista, J.L. (1999). Incorporation of yttrium in barium titanate ceramics. *J. Am. Ceram. Soc.* 82 (5), 1345–1348. https://doi.org/10.1111/j.1151-2916.1999.tb01921.x.